IIETA International Information and Engineering Technology Association
Advancing the World of Information and Engineering

Revue des Composites et des Matériaux Avancés-Journal of Composite and Advanced Materials
Vol. 36, No. 1, February, 2026, pp. 27-39
Journal homepage: http://iieta.org/journals/rcma

Optimizing p-n Heterojunction Interfaces: Enhanced Room-Temperature Ammonia Sensing of Polyaniline/α-Fe_2O_3 Nanocomposites

Shehabaddin A. Khaleefah[1,2*], Asghar Esmaeili[2]

[1] Scientific Research Commission, Baghdad 10070, Iraq
[2] Faculty of Science, Department of Physics, Urmia University, Urmia 5756151818, Iran

Corresponding Author Email: shehabaddin.a.khaleefah@src.edu.iq

https://doi.org/10.18280/rcma.360103

Received: 1 September 2025
Revised: 30 November 2025
Accepted: 14 February 2026
Available online: 28 February 2026

Keywords:
polyaniline, α-Fe_2O_3, p-n heterojunction, ammonia gas sensor, room-temperature sensing, chemiresistive

ABSTRACT

Ammonia (NH_3) leakage in industrial settings poses severe health and environmental risks, necessitating high-performance sensors capable of reliable operation at room temperature. While polyaniline (PANI) offers solution-processability and tunable conductivity, its pristine form suffers from low sensitivity and sluggish response kinetics. Here, we report a high-performance room-temperature NH_3 sensor based on PANI/α-Fe_2O_3 nanocomposites synthesized via a one-step chemical bath deposition method. We systematically investigate the critical role of α-Fe_2O_3 nanoparticle loading (1, 3, and 5 wt.%) in tailoring the morphological, structural, optical, and electrical properties of the hybrid film. Structural and microscopic analyses reveal that an optimal loading of 3 wt.% α-Fe_2O_3 induces the formation of well-dispersed p-n heterojunctions, maximizing the specific surface area and creating abundant charge-transport pathways. Consequently, this optimized composite exhibits a superior sensing response of 86.96% toward 50 ppm NH_3 at room temperature, with rapid response/recovery times (48 s/48 s)—a significant enhancement compared to both pristine PANI and non-optimized composites. The enhanced performance is attributed to the synergistic modulation of the depletion layer width at the heterojunction interface upon NH_3 adsorption, facilitating efficient charge transfer. This work not only identifies the optimal composition for PANI/α-Fe_2O_3 based sensors but also provides a fundamental understanding of the loading-dependent synergistic effects, offering a rational design strategy for next-generation, low-power chemiresistive gas sensors.

1. INTRODUCTION

The rapid advancement of technological systems has led to vast vehicular emissions, improper waste management policies, and domestic daily activities, all of which are considered significant sources of environmental pollutants [1]. Monitoring these contaminants is critical to mitigating ecological degradation and safeguarding public health. Gas sensors have emerged as pivotal tools in both industrial and research settings, owing to their ability to detect airborne toxic compounds that pose substantial risks to human health [2]. Prolonged exposure to hazardous gases like carbon monoxide (CO), nitrogen oxides (NO, NO_2), In addition to volatile organic compounds (VOC) can lead to respiratory disorders (e.g., asthma and hypoxia), skin irritation, neurological symptoms (dizziness, drowsiness), gastrointestinal distress (nausea, vomiting), besides the chronic conditions, like carcinogenic effects and pulmonary dysfunction [3]. Regulatory frameworks were established in which the threshold limit values (TLVs) for gaseous pollutants were specified as the maximum permissible atmospheric concentrations, that is typically expressed as parts per million (ppm), considered safe for human exposure. Figure 1 shows the dose-dependent health effects of toxic gas inhalation, underscoring the urgent need for real-time air quality detection systems.

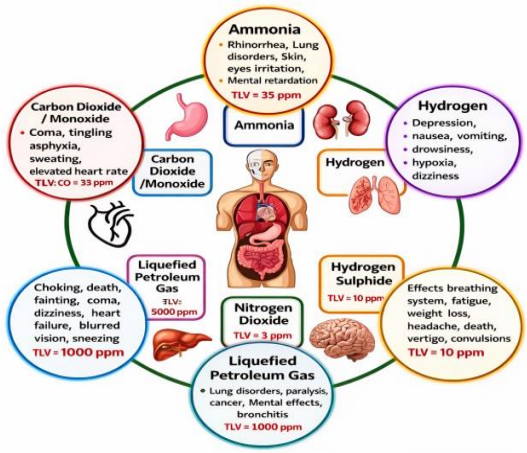

Figure 1. The health impacts of toxic gases on humans

These gases are emitted from two main sources: natural emissions (e.g., volcanic activities) and artificial activities (e.g., industrial processes). Gas sensors convert chemical interactions with target toxic gases into measurable electrical signals, enabling real-time monitoring [4]. One of the important industrial gases is ammonia, which is considered a very dangerous gas because of its toxicity even at very low concentrations.

1.1 Ammonia toxicity

Ammonia (NH_3) is a toxic, colorless gas that poses significant health risks and requires monitoring in medical, industrial, and residential settings. This inorganic compound plays a crucial role in atmospheric, industrial, and biological systems. It is widely utilized across numerous sectors, such as fertilizer manufacturing. detergent products, petroleum refining products, electricity power generation, the rubber industry, food processing, pharmaceuticals, and the automobile sector [5]. However, these industrial applications carry a substantial risk of NH_3 being liberated into the air, leading to serious pollution issues. Even at low concentrations, ammonia can cause skin irritation, ocular discomfort, and irritation of the upper respiratory tract. In addition, this gas may cause dizziness, fatigue, and nausea. At high concentrations, ammonia can lead to harmful consequences, such as cardiac arrest and damage to the reproductive system. The permissible exposure limit for this gas is about 35 ppm for 15 minutes exposure period and 25 ppm as an average over an 8-hour workday, beyond which it poses a clear risk to human health according to the U.S. Occupational Safety and Health Administration (OSHA) [6].

In summary, the ability to achieve high sensitivity detection of NH_3 gas, instant response, accuracy, and reliable performance at room temperature has become essential for healthcare diagnostics, and for industrial safety, in addition to environmental monitoring [7].

Sensors are effective techniques to detect toxic gases. Various types are used with different mechanisms based on the nature of the gas itself, besides the characteristics of every gas. So, this field has witnessed rapid developments to match the fast developments in industrial sectors and to control the toxic gas emissions [8].

The last developments in the sensor industry have increasingly focused on the conductive polymer (CP) such as polyaniline (PANI), which has gained increasing attention in recent times because of the simple and easy synthesis method, adjustable electrical conductivity, and it can work at room temperature. Despite these merits, pure PANI-based sensors show some limitations, such as mild sensitivity, moderate response and recovery duration, in addition to their low selectivity. On the other hand, metal oxides exhibit high thermal stability and high sensitivity, but these oxides need elevated operation conditions, which may on ammonia detection process [9].

To take the utmost benefit of the properties of both, Hybrid composites including PANI and metal oxide have been classified as a promising strategy. In this hybrid composite system, the PANI enhances the electrical conductivity and the mechanical flexibility, while the metal oxide with high surface and strong adsorption sites for ammonia molecules will strengthen the synergistic interaction, leading to improved sensor performance and other sensing properties [10]. The polyaniline (PANI) integrated with metal oxide nanoparticles (e.g., α-Fe_2O_3) has shown exceptional and promising sensing materials. These hybrids capitalize on inherent redox characteristics, tunable electrical conductivity, and the ambient operational stability [11].

Despite all these merits and developments in conductive polymer (CP)/metal oxide nanoparticles, there are challenges, such as fast response, low concentration detection, and high selectivity of ammonia gas. Furthermore, the systematic investigations that focus on the conductive polymer (CP)/metal oxide nanoparticles are still limited and require a deeper understanding to reach an effective design of a high-performance ammonia sensor.

1.2 Gas sensing principles

Chemical sensors operate by detecting the interactions between target gas and sensing materials, which induce the measurable variations in the physical properties, such as electrical resistance, current magnitude, optical absorbance, or mass variation [12]. In conductive polymer (CP) based sensors, key performance metrics, including sensitivity and response kinetics, are enhanced by optimizing the charge transfer dynamics at the gas/polymer interface [13]. These sensors are classified based on their transduction mechanisms, which are controlled by physicochemical interactions between the CP matrix and the gas. These interactions are either chemical redox reactions or physical adsorption that are powerfully affected by the doping state of the polymer, which modulates its electronic structure and charge transport behavior [14]. The doping process works on inserting the charge carriers into the conductive polymer (CP) framework, thereby tuning its conductivity and changing its affinity for specific gas molecules. Upon gas exposure, chemo-electrical transduction happens by gas molecule adsorption or interfacial charge transfer, leading to the generation of detectable physical or electrochemical signals proportional to gas concentration. So, the operational efficiency of sensors is directly governed by the doping level. Besides, sensor activity is controlled by the active sites and the energy barrier for charge exchange during the sensing process [15].

The sensing mechanism mainly depends on the direct interactions of charge transfer of the polymer surface with gas molecules. The inorganic compounds, such as metals or metal oxides, show catalytic activity upon exposure to the target gas. When these oxides are embedded into a polymeric matrix to form nano-hybrids, these nanocomposites demonstrate enhanced gas sensing performance because of synergistic effects [16]. The nanohybrid structure offers plentiful active sites besides a high surface area, enhancing the gas adsorption efficiency. Also, the polymer matrix restrains the inorganic nanoparticles' agglomeration, while the inorganic compounds prevent polymer degradation, thereby ensuring long-term structural stability [17].

Upon exposure to ambient conditions, atmospheric oxygen adsorbs onto the metal oxide surface, acquiring electrons from its conduction band to form ionized oxygen species (e.g., O_2^{2-}, O^{2-}). This process generates a charge-depletion layer at the oxide surface, which increases the electrical resistance. When the sensor interacts with the target gases, the adsorbed oxygen reacts with the analyte molecules and releases electrons into the conduction band. This electron exchange reduces the width of the depletion layer, thereby modulating the sensor's conductance [18, 19].

Heterojunctions formed between n-type metal oxides and p-

type polymers play a critical role in conductivity modulation. Due to the lower Fermi energy level of metal oxides relative to polymers, electrons transfer from the inorganic phase to the polymeric phase until Fermi-level alignment is achieved. This redistribution reduces the electron density at the oxide surface and interface, elevates the potential barrier, and expands the depletion layer, thereby amplifying the resistance changes [20].

Sensor response dynamics depend on the semiconductor type: n-type materials exhibit increased conductance upon exposure to electron-donating (reducing) gases and decreased conductance when exposed to electron-withdrawing (oxidizing) analytes [21]. Conversely, p-type semiconductors display the opposite behavior, where oxidizing gases enhance conductivity by increasing the hole concentration, while reducing gases diminish it. A comprehensive understanding of these charge-transfer mechanisms and heterostructure interactions is essential for optimizing sensor selectivity and sensitivity in practical applications [22].

The sensing reactions predominantly occur on the sensor layer surface. These reactions take place on the sensor surface, the thin polymer films, as shown in Figure 2. The sensor's sensitivity is mainly depended on the size of the semiconductor particles, which is one of the primary requirements for enhancing the sensor performance. The sensor sensitivity can be defined as the relative change in the resistance of the sensitive thin film, expressed as a percentage per ppm of the applied gas concentration, as shown in Eq. (1):

$$S = \frac{(R_g - R_a)}{R_a} \times 100\% \quad (1)$$

where, R_a is the electrical resistance of the sensor in air, while R_g are and the presence of gas.

1.3 Response and recovery times

A gas sensor's response time (τ_{res}) is the time required for the sensor to reach 90% of its maximum or minimum conductance value upon exposure to a reducing or oxidizing gas. Conversely, the recovery time (τ_{rec}) is the interval needed for the sensor to return to within 10% of the original baseline once the reducing or oxidizing gas flow is stopped. Figure 3 illustrates this measurement by plotting conductance versus time based on the sensor data [23].

Table 1 shows the responses of the sensing elements towards oxidizing and reducing gases and their behaviour according to the type of semiconductor elements either n- or p-type.

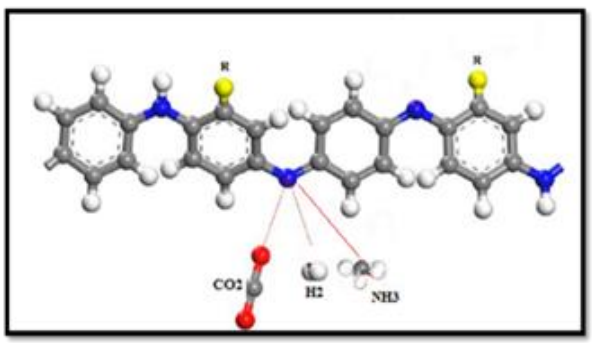

Figure 2. The sensing reaction on the polymer surface

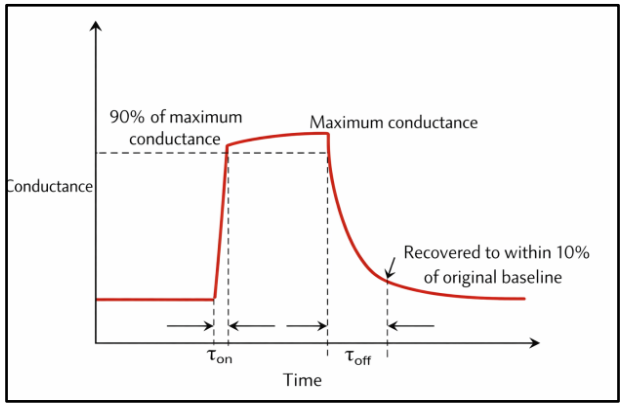

Figure 3. Response and recovery times

Table 1. The response of the sensing elements

Classification	Oxidizing Gases	Reducing Gases
n-type	Resistance increase	Resistance decrease
p-type	Resistance decrease	Resistance increase

This work focuses on investigating the structure- property relationship of PANI doped with different loadings of A-Fe_2O_3 nanoparticles (1 wt.%, 3 wt.%, and 5 wt.%). The sensor will be synthesized, and then it will be characterized using different tests to investigate the structural, morphological, and elemental composition in addition to its performance as an NH_3 sensor will assess reaching the optimal ratio.

2. EXPERIMENTAL SECTION

2.1 Materials and equipment

The materials, chemicals, and equipment that were used in this work are listed in Tables 2 and 3.

2.2 Polyaniline preparation

Initially, pure polyaniline (PANI) was synthesized using readily available chemicals as follows:

1> Aniline hydrochloride solution was prepared by mixing 2.7 g with 50 mL of DW. This solution was coded A.
2> Parallelly, APS solution was synthesized by dissolving 5.7 g in 50 mL of DWin in order to obtain the ratio of 1:2. This solution was coded B.
3> The two solutions was stirrred seperately for 60 minutes at room temperature.
4> The solution B was added to solution A drop by drop as shown in Figure 4 with stirring at room temperature for 60 minutes.
5> Next, the glass slides that were cleaned with aliquots of 0.2 M HCl and acetone were subsequently immersed in the solution to create thin-film samples using a chemical deposition method (sol–gel dip coating) for 24 hours at room temperature.
6> After they were removed and dried at room temperature, they were stored in a desiccator for characterizations and sensing performance tests.

Table 2. Physical properties of compounds

No.	Chemicals	Molecular Formula	M. wt (g·mol^{-1})	Purity (%)	Source
1-	Ammonium Persulphate (APS)	$(NH_4)_2 S_2 O_8$	228.19	99	CDH
2-	Aniline hydrochloride	$C_6H_5NH_3$ HCL	129.6	99	MACKLIN
3-	Hydrochloric acid	HCL	36.46	98	FLUKA
4-	α -Ferric oxide	Fe_2O_3	159.7	99	MACKLIN
5-	Acetone	C_3H_6O	58.08	> 98	BDH

Table 3. The work instruments

No.	Type of Device	Origin	Model
1-	Ultrasonic cleaner	China	------
2-	Electric Balance	China	-------
3-	Heating.Magnetic Stirrer	Taiwan	--------
4-	Power Supply	Japan	--------
5-	Grinding and Polishing	Denmark	KNUTH-ROTOR-2
6-	Optical Microscope	Japan	Nikon.Eclipse ME600
7-	Water bath	Germany	HAM Burg
8-	Fourier transform infrared spectroscopy (FT-IR) spectroscopy	Japan	Shimadzu FTIR- 8400
9-	Thermal analyzer	Japan	Shimadzu TGA-60 DSC
10-	Vacuum evaporation	Germany	Thermionic
11-	X-ray diffraction (XRD)	Japan	Shimadzu-6000
12-	Energy Dispersive X-ray Spectroscopy (EDS)	USA	Autolab /FRA 4.9
13-	Hall Effect Measurement System	China	Ecopia(HMS-3000)
14-	Surface area analyzers	KOREA	HORIBA SA-9600
15-	Gas Sensor System	China	------
16-	Ultraviolet-visible spectroscopy (UV-vis)	Japan	Shimadzu3600

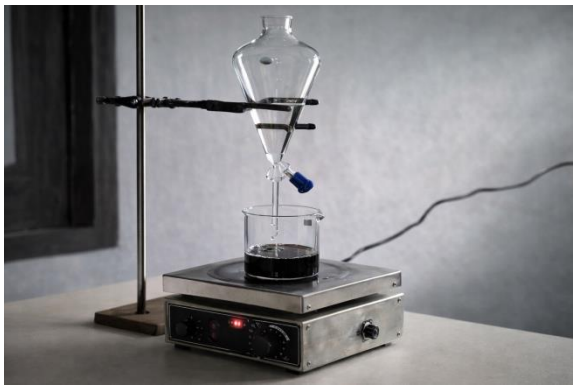

Figure 4. Polyaniline (PANI) preparation

2.3 Iron oxide/Polianile composite preparation

First, the polyaniline solution was prepared as described in 2.2. Meanwhile, the metal oxide (α-Fe_2O_3) dispersion was prepared by adding (α-Fe_2O_3) to the polyaniline solution at three different concentrations (1, 3, and 5% wt.%) and stirring for 60 minutes to achieve better homogeneity. After, the glass slides were immersed in the solution to create thin-film samples using a chemical deposition method (sol–gel dip coating) for 4 hours at room temperature. The active layer of the conducting polymer, functioning as the sensing element, reacts with gas molecules and produces a corresponding change in conductivity. Figure 5 shows the deposition system.

2.4 Preparation of masks and electrode deposition

Figure 6 shows the preparation of masks from aluminum foil. Aluminum sheets were used to achieve the desired electrode shapes. These masks precisely matched the dimensions of the substrates and were fixed onto the cleaned substrates. The masks were then placed on the films to deposit aluminum onto the PANI film surface, utilizing the vacuum thermal evaporation method with a tungsten (W) boat under a pressure of 10^{-5} Torr. The width of the aluminum electrode was 2 mm.

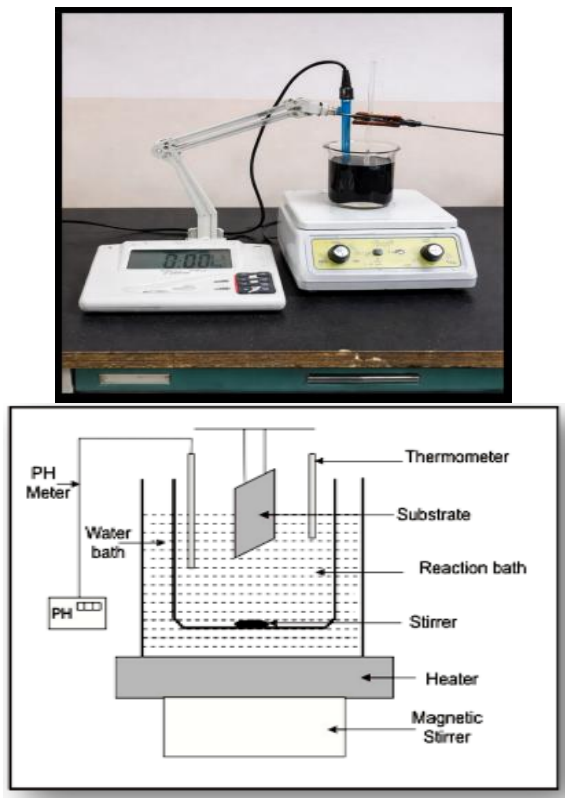

Figure 5. The chemical bath deposition (CBD) deposition system

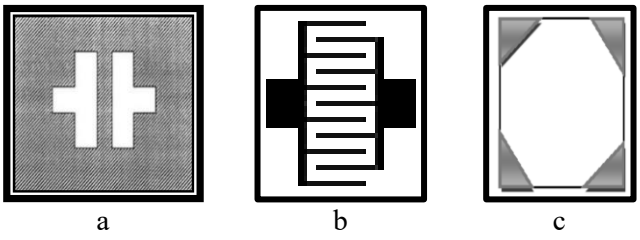

Figure 6. Mask pattern used in electrical measurements: (a) DC conductivity, (b) Gas sensing, (c) Hall effect

2.5 Thin film sensitivity measurements

The gas sensor sensitivity was tested and measured using the gas sensor system, as shown in Figure 7. The synthesized sensors were investigated to detect 50 ppm of ammonia. The specified NH_3 gas concentration is utilized with a gas mixing system combined with mass flow meters. The pure NH_3 was diluted with dry air. The flow rates of both gases were precisely adjusted and calibrated to an accurate targeted concentration (50 ppm).

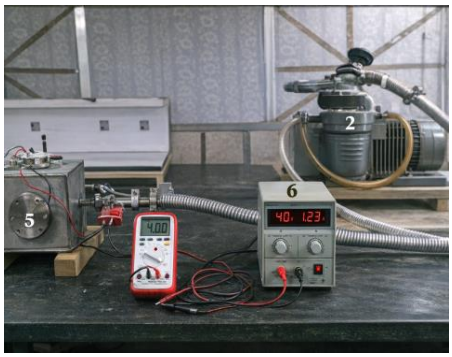

Figure 7. Gas sensor system

3. RESULTS AND DISCUSSION

3.1 X-ray diffraction test

Figure 8 shows the structures of pure PANI, α-Fe_2O_3, and their composites. The thin films were analyzed using X-ray diffraction (XRD-6000, Shimadzu, Japan) with Cu Kα radiation (λ = 1.54 Å). The results show broad diffraction peaks between 10° and 30°, which can be attributed to the parallel and vertical periodicity of the PANI chains. The PANI peaks indicate low crystallinity due to the repetitive quinone and benzene rings in the polymer chains. The three main pristine PANI peaks at 2θ = 18.11°, 23.75°, and 26.50° correspond to the (011), (020), and (200) planes, respectively. In contrast, pure A-Fe_2O_3 peaks appear at 2θ = 18.21° and 23.84°. For the composites, 1% A-Fe_2O_3 shows peaks at 2θ = 24.75° and 32.96°, while the dominant peaks of the 3% A-Fe_2O_3 composite appear at 2θ = 23.80° and 32.93°. Finally, the 5% A-Fe_2O_3 composite exhibits peaks at 2θ = 23.86° and 32.41°.

The crystallite sizes were calculated utilizing the Scherrer equation, showing that the average crystallite size of pure polyaniline is 15.68 nm, while that of the composite with 1% A-Fe_2O_3 is 15.95 nm. For the composite with 3% Fe_2O_3, the average crystallite size is 19.99 nm, and for the composite with 5% Fe_2O_3, it is 19.94 nm.

The important notes that can be summarized from the XRD test can be listed below as follows:

1> At 1% (α-Fe_2O_3) NPs, the crystallite size was close to the pure PANI crystallite due to oxide seeds that began to interact with crystalline domains

2> At 3% (α-Fe_2O_3) NPs, there are sufficient nuclei and local Fe ions during polymerization, so crystallites can grow more freely, leading to a larger size. In this stage, Nps plays as nucleating and growth agents for polymer chains to align around them.

3> At 5% (α-Fe_2O_3) NPs, the reduction in crystallite size can be attributed to NPs agglomeration and particle-particle interface instead of particle-polymer interaction, leading to a reduction in crystallite size.

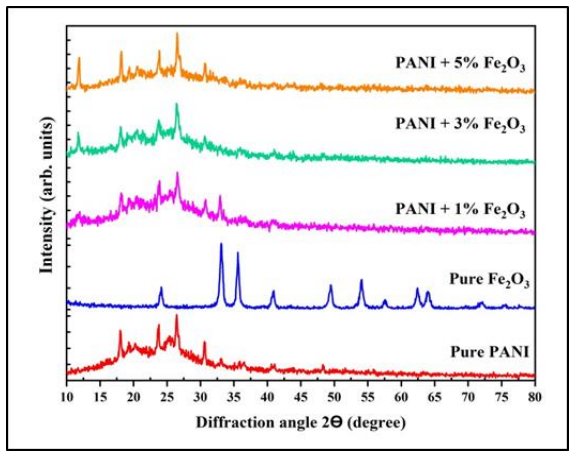

Figure 8. X-ray diffraction (XRD) of PANI/iron oxide composites

3.2 Fourier transform infrared spectroscopy

FT-IR analyses were conducted to investigate the molecular structure of the synthesized PANI/α-A-Fe_2O_3 thin films. The polymer formation, the presence of functional groups on the polymer backbone, and changes in the protonation–deprotonation equilibrium of emeraldine can be inferred from the corresponding bonds in the FT-IR spectrum. Figure 9 summarizes the infrared spectra of pure PANI and its nanocomposites. The key functional groups are observed in the following:

1> The band at 3447 cm^{-1} belongs to the C-H stretching vibration.

2> The bands at 1565 cm^{-1} and 1480 cm^{-1} belong to the C = N and C = C stretching That both indicte to presence of the benzoid and quinoid units, respectively.

3> The band at 1303 cm^{-1} is the characteristic one of the polyaniline spectrum because of C-N stretching mode of the benzene units.

4> The band at 1141 cm^{-1} is considered a characteristic band of PANI (protonation band). It is known as the protonated N atom in the benzenoid unit.

5> The bands at 878, 809, and 698 cm^{-1} indicate the C-H in-plane bending vibration and C-H out-of-plane bending vibration of the benzene ring, respectively.

6> After the addition of nanoparticles, the important points are:

a. - At 1% α-A-Fe_2O_3 NPs: The peaks of pure PANI remain clearly visible, although with a slight reduction in intensity. Additionally,

a new weak peak appears at 454 cm^{-1}, belonging to the Fe–O bond, indicating the presence of A-Fe_2O_3 nanoparticles. A small shift in the C–N bond is also observed, suggesting initial interactions between Fe and PANI.

b. - At 3% α-A-Fe_2O_3 NPs: The prominent observation is that the bands in the 439–616 cm^{-1} range become stronger, indicating a higher loading of A-Fe_2O_3 nanoparticles. Additionally, the quinoid peak shifts from 1556 to 1610 cm^{-1}, reflecting enhanced coordination and stronger interactions between the metal oxide nanoparticles and the polymer matrix.

c. - At 5% α-A-Fe_2O_3 NPs: The band at 439 cm^{-1} remains strong, indicating the presence of the Fe–O bond. Notably, the characteristic PANI peaks at 1565–1480 cm^{-1} become weaker than before, suggesting that the nanoparticles partially cover the polymer chains. Furthermore, the excess metal oxide slightly reduces the degree of protonation, leading to a conductivity reduction, as reflected in the sensing experiments.

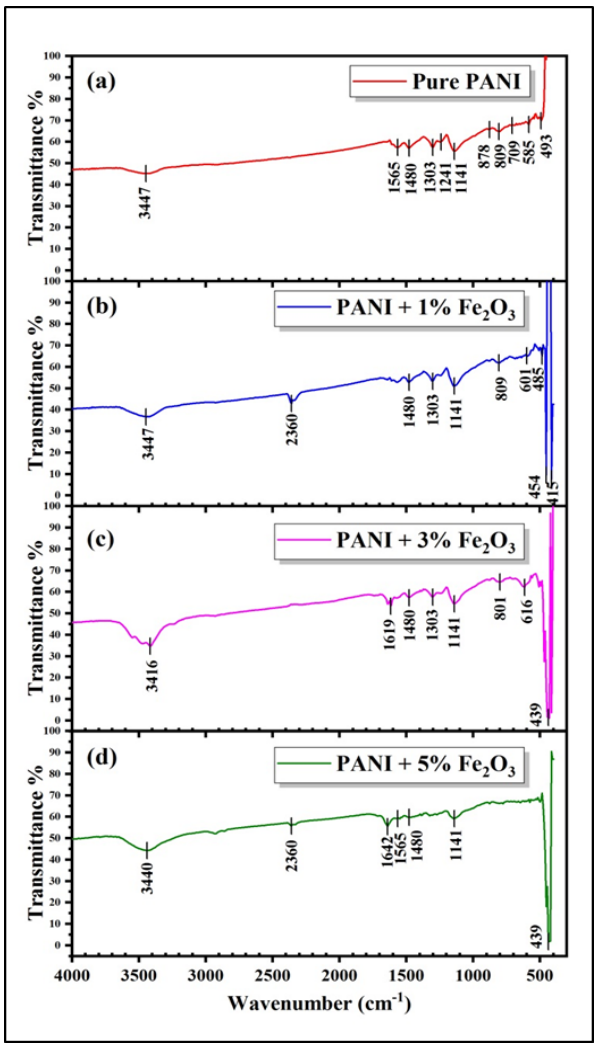

Figure 9. Fourier transform infrared spectroscopy (FTIR) spectrums of PANI/iron oxide composites

3.3 Ultraviolet-visible spectroscopy test results

The ultraviolet-visible spectroscopy (UV-vis) technique is considered as one of the most important techniques for characterizing and determining the conformational structures and electrical properties of conducting polymers (CPs), including their energy gap (Eg). CPs possess an extended arrangement of alternating single and double bonds, allowing them to absorb light in the ultraviolet and visible regions, typically between 290 and 900 nm.

Figure 10 illustrates the UV–vis spectra of pristine PANI and PANI/A-Fe_2O_3 composites with three weight percentages (1%, 3%, and 5%). These spectra are vital for assessing the degree of conjugation. Strongly conjugated and conductive polyaniline samples show a broad absorbance, known as a free carrier tail, at wavelengths beyond approximately 700 nm. As the length of conjugation increases, the peaks shift to longer wavelengths and intensify, as observed in the UV-vis spectrum of chemically synthesized PANI.

Typically, the emeraldine base exhibits an absorbance around 330 nm, belonging to the benzenoid π–π* transition, and around 635 nm, due to quinoid exciton absorption. After doping, the quinoid transition does not appear, and two new absorbances emerge, corresponding to polaron and bipolaron transitions. The polaron transition appears at a higher wavelength (lower energy) than the bipolaron transition. The conducting emeraldine salt exhibits two characteristic absorption bands at 320–328 nm and 420–440 nm. The peak at 320 nm corresponds to the π–π* transition of the benzenoid ring, while the sharp trough is attributed to localized polarons, characteristic of protonated polyaniline, with extended absorbance at 700–800 nm indicating to the conducting electronic state of PANI.

These spectra provide strong evidence for the protonation of PANI. Absorbance values increased with increasing membrane thickness and decreased with increasing wavelength, while transmittance values decreased with increasing thickness and increased with wavelength increasing. This behavior is matching with the equation ($\alpha = 2.303\ A/t$), where absorbance (A) is directly proportional to the absorption coefficient. It was also observed that absorbance values decreased after annealing, whereas transmittance values increased, which is attributed to particle size increase and corresponding changes in the material's optical properties after annealing.

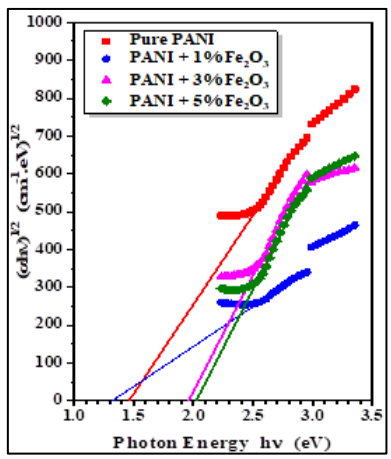

Figure 10. Ultraviolet-visible spectroscopy (UV-vis) test of PANI/iron oxide composites

Table 4 shows the energy band gaps of pure PANI and its composites with three A-Fe_2O_3 weight percentages (1%, 3%, and 5%), which are 1.46, 1.32, 1.96, and 2.02 eV, respectively. It is noted that the band gap increases with increasing A-Fe_2O_3 content. This is because the higher doping ratio introduces new localized energy levels near the top of the valence band and the bottom of the conduction band. These levels can trap electrons and generate tails within the forbidden energy gap.

Table 4. The energy gaps of SH1, SH2, SH3, and SH4

Sample	Thickness (nm)	Concentration	Eg (eV)
SH1	135.4	Pure PANI	1.46
SH2	175.7	PANI+ 1% α-Fe_2O_3	1.32
SH3	230.1	PANI+ 3% α-Fe_2O_3	1.96
SH4	250.2	PANI+ 5% α-Fe_2O_3	2.02

The results of this test reveal a non-monotonic trend in the optical band gap values with increasing α-A-Fe_2O_3 NPs content.

1> The film thickness increased according to the matal oxide doping ratio, consistent with an accurate dip coating process.
2> At 1% addition, the energy gap decreased to 1.32 eV compared to 1.46 eV for pure PANI. This behavior can be attributed to the ease of charge transfer.
3> At 3%, the energy gap significantly increased (1.96 eV), indicating a higher energy barrier for electron-hole pair separation for interacting with NH_3 molecules.
4> At 5% NPs addition, the nanoparticles tend to agglomerate, reducing polymer conjugation and introducing excessive NPs that immobilize charge carriers, thereby decreasing conductivity.

3.4 Electrical measurements - Hall effect

The Hall effect is a transverse voltage generation in a conductive or semiconductive strip when exposed to a magnetic field. By studying the Hall effect, one can determine the type of semiconductor (n-type or p-type) as well as key electrical properties such as carrier mobility, majority charge carrier concentration, and conductivity $R_H = 1/ne$. This equation is fundamental because knowing both the magnitude and sign of RHR_HRH allows the determination of the density and type of charge carriers contributing to conduction. A semiconductor is classified as n-type if RH is negative, indicating that electrons are the majority carriers. Conversely, it is classified as p-type if RH is positive, referring to the majority carriers are in holes. In addition, the Hall mobility (μH) can be calculated from the relationship between the Hall coefficient and conductivity (σ), as shown in Eq. (2). The Hall effect results are summarized in Table 5.

$$\mu_H = |R_H|\sigma \quad (2)$$

Table 5. Hall measurement of thin film samples

Sample #	Average Hall Coefficient (m^2/C)	Mobility (Cm^2/Vs)	Conductivity (S/cm)	Resistivity (Ω.cm)
SH1	$-1.47 \times 10^{+9}$	$2.21 \times 10^{+1}$	1.5×10^{-8}	$6.63 \times 10^{+7}$
SH2	$-5.109 \times 10^{+8}$	$6.59 \times 10^{+1}$	1.29×10^{-7}	$7.74 \times 10^{+6}$
SH3	$-1.55 \times 10^{+10}$	$1.24 \times 10^{+3}$	7.99×10^{-8}	$1.251 \times 10^{+7}$
SH4	$-1.132 \times 10^{+9}$	$2.59 \times 10^{+1}$	2.292×10^{-8}	$4.362 \times 10^{+7}$

As shown in Table 3, the Hall measurements indicate that the electrical properties of the composites improved with the addition of α-Fe_2O_3 at the three weight percentages (1%, 3%, and 5%). Additionally, the electrical resistance decreased due to the metal oxide role, which reduces the energy band gap and facilitates electron transfer between the valence and conduction bands across the p–n junction. The highest conductivity values were observed for the 3% and 5% A-Fe_2O_3 additions. It is also noted that the Hall coefficient signs are negative for most of the samples, indicating n-type behavior.

3.5 Scanning electron microscopy

SEM was utilized to investigate the morphology and surface structure of the pure and composite samples. The shape and size of the particles have a direct impact on the morphological characteristics. SEM analysis, combined with image processing software, was employed to specify the particle shape and size. The pure PANI morphology is shown in Figure 11. At a magnification of 50 μm, the image reveals clusters of polymeric PANI particles with clearly defined, large, and irregularly sized particles. At 20 μm, these clusters appear randomly arranged, closely packed, and with various shapes. At a lower magnification of 5 μm, the clusters appear larger and more randomly distributed.

For the addition of iron oxide (α-Fe_2O_3), as shown in Figure 12 for the 1% addition rate, the SEM image at 50 μm magnification shows thin, overlapping sheets of α-Fe_2O_3 distributed relatively randomly in all directions, with little porosity due to the low addition rate. At 20 μm magnification, the lamellar structure is visible as thin threads interconnected in all directions, covering the surface completely. At higher magnification (2 μm), the particles appear to interact closely with the polymer matrix, enhancing the electrical and conductive properties of the composite.

When 3% iron oxide was added to the composite, as shown in Figure 13, the surface appeared more uniform. The particle size was measured to be less than 100 nm, and the surface area increased. This structural improvement contributed to a noticeable enhancement in conductivity and overall electrical properties. As shown in Figure 13, the surface morphology of the SH3 sample shows a more uniform nanoparticle distribution and fewer agglomerates than in Figure 12. The higher magnification of Figure 13 further shows that these particles exhibit an interconnected network structure, which facilitates electron conduction.

When 5% iron oxide (α-Fe_2O_3) was added to the composite, as shown in Figure 14, the 20 μm magnification image reveals a sequential arrangement of small particles linked to the polymer chains, with a homogeneous distribution between the composite components. At higher magnification (1 μm), the particle size was measured to be less than 100 nm. This improved structure contributed to enhanced electrical properties, including increased carrier mobility and

conductivity.

The morphology of the nanocomposite samples has a crucial effect on gas sensing performance. Homogeneous particle distribution and small particle sizes provide more active sites on the surface for interaction with gas molecules, resulting in higher sensing efficiency.

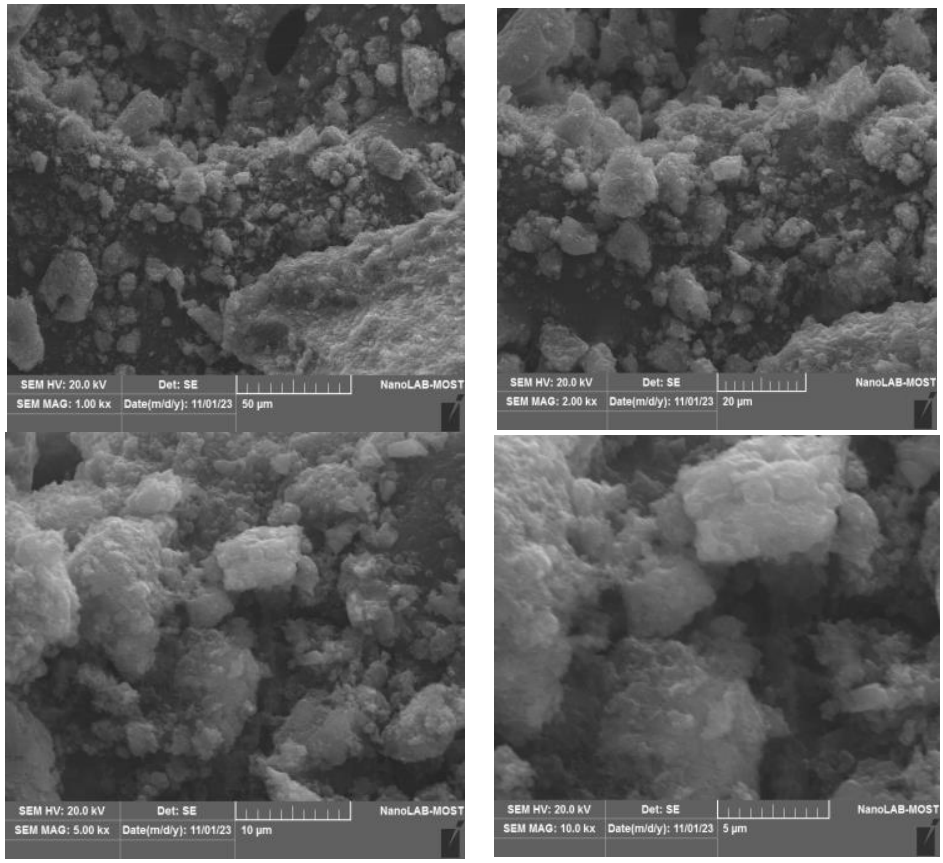

Figure 11. Scanning electron microscopy (SEM) images for SH1 sample

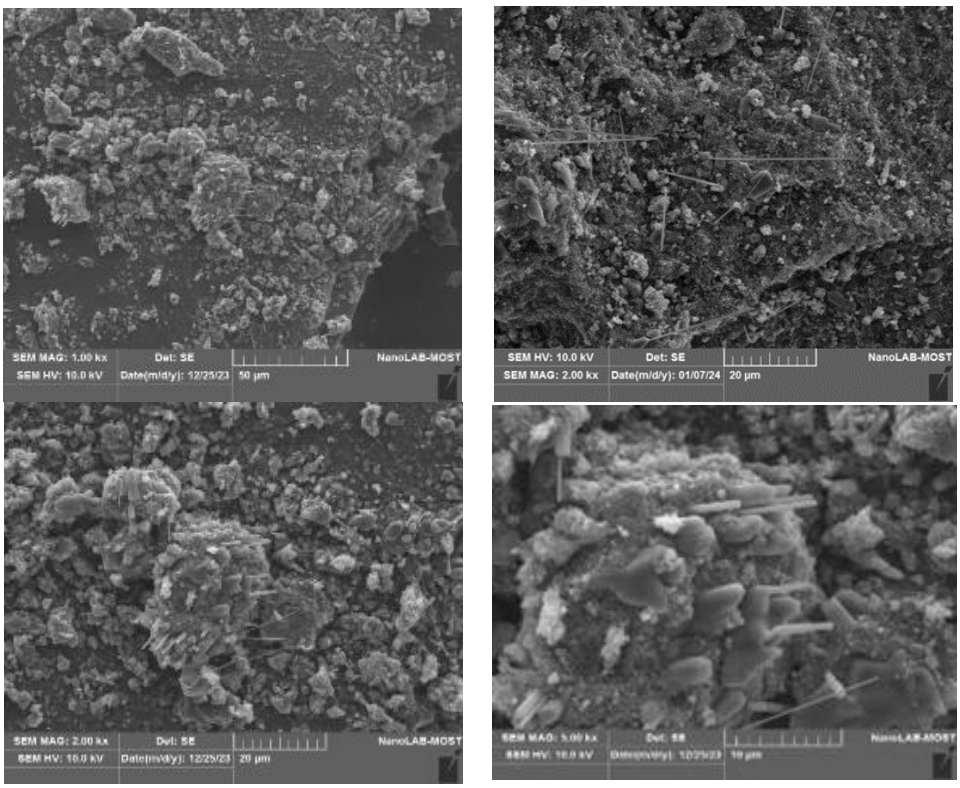

Figure 12. Scanning electron microscopy (SEM) images for SH2

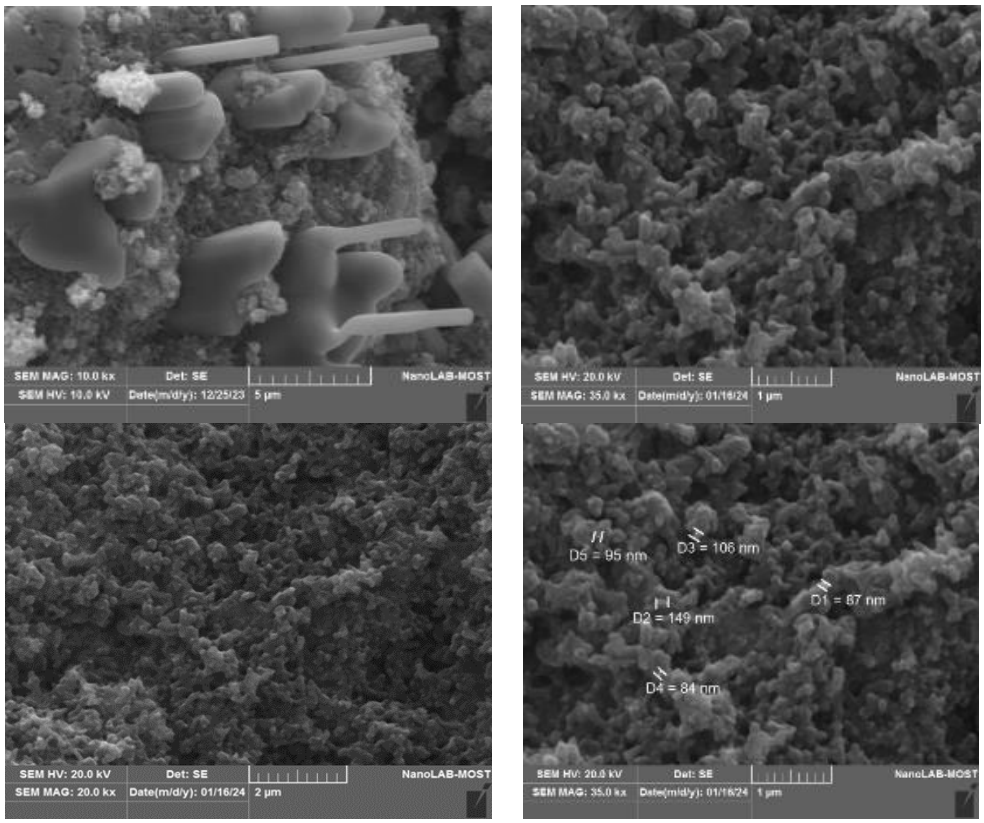

Figure 13. Scanning electron microscopy (SEM) images for SH3 sample

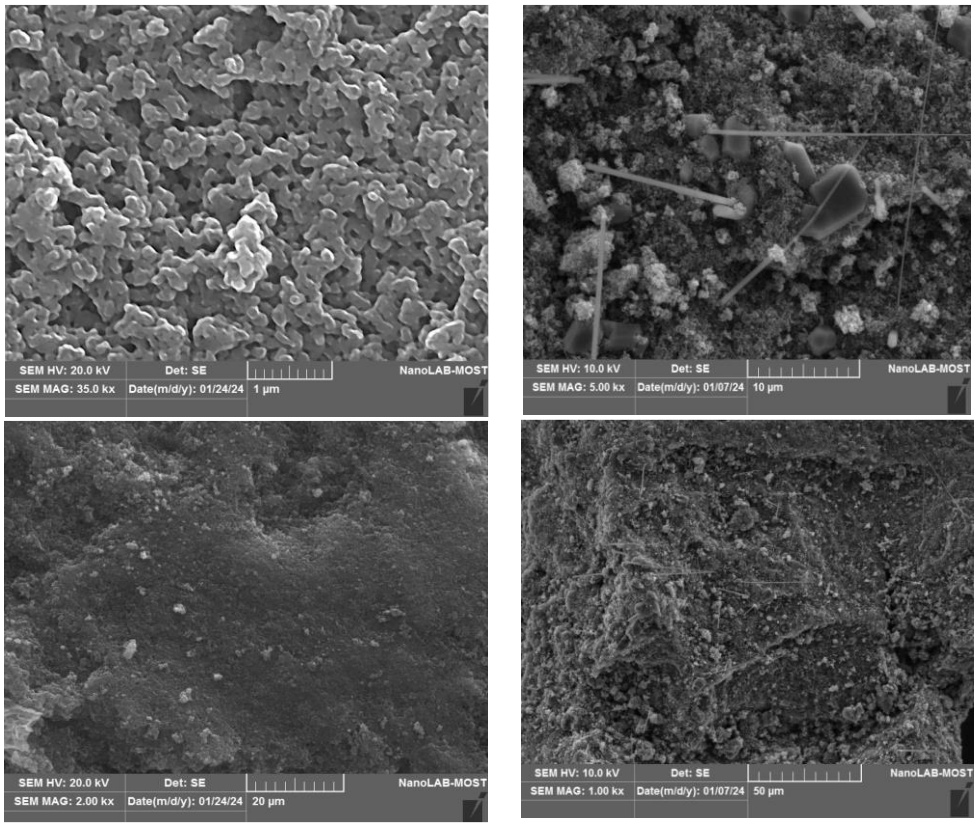

Figure 14. Scanning electron microscopy (SEM) images for SH4 sample

3.6 Energy dispersive X-ray analysis system (energy-dispersive X-ray spectroscopy)

Figure 15 shows the results of the Energy-dispersive X-ray spectroscopy (EDS) analysis. The primary chemical elements appearing in this test extract were determined according to their percentage of the total and according to the table attached to each sample.

SH1 (Pure PANI): elements (C, O, Cl, S, N)

SH2 (PANI +1% Fe_2O_3): Appearing elements (Fe, C, O, CI,

S, N)

SH3 (PANI + 3%: Appearing elements (Fe, C, O, CI, S, Si, N, Al)

SH4 (PANI + 5% Fe_2O_3) Appearing elements are (Fe, C, O, Cl, N, S, Si, Ca, and K)

3.7 Sensitivity calculations

The n-type gas sensor is preferred over the p-type sensor because its resistance decreases from maximum to minimum in the existence of gas, whereas the p-type sensor's resistance increases. While, in the n-type semiconductors, oxygen ions (O_2^-) adsorb on the surface at the grain boundaries, reducing the charge carrier concentration and increasing the potential barrier, which impedes carrier movement. When exposed to an oxidizing gas, such as NO_2, the thin film absorbs oxygen ions at the grain boundaries, further decreasing the charge carrier concentration. This increases the resistance of the thin film and reduces its conductivity. Conversely, exposure to a reducing gas, such as NH_3, H_2S, or H_2, decreases the adsorbed oxygen ions on the surface, increasing the charge carrier concentration, lowering the potential barrier, decreasing resistance, and enhancing conductivity. Sensitivity was calculated using Eq. (3):

$$S = \left|\left(R_g - R_a\right)/R_a\right| \times 100\% \quad (3)$$

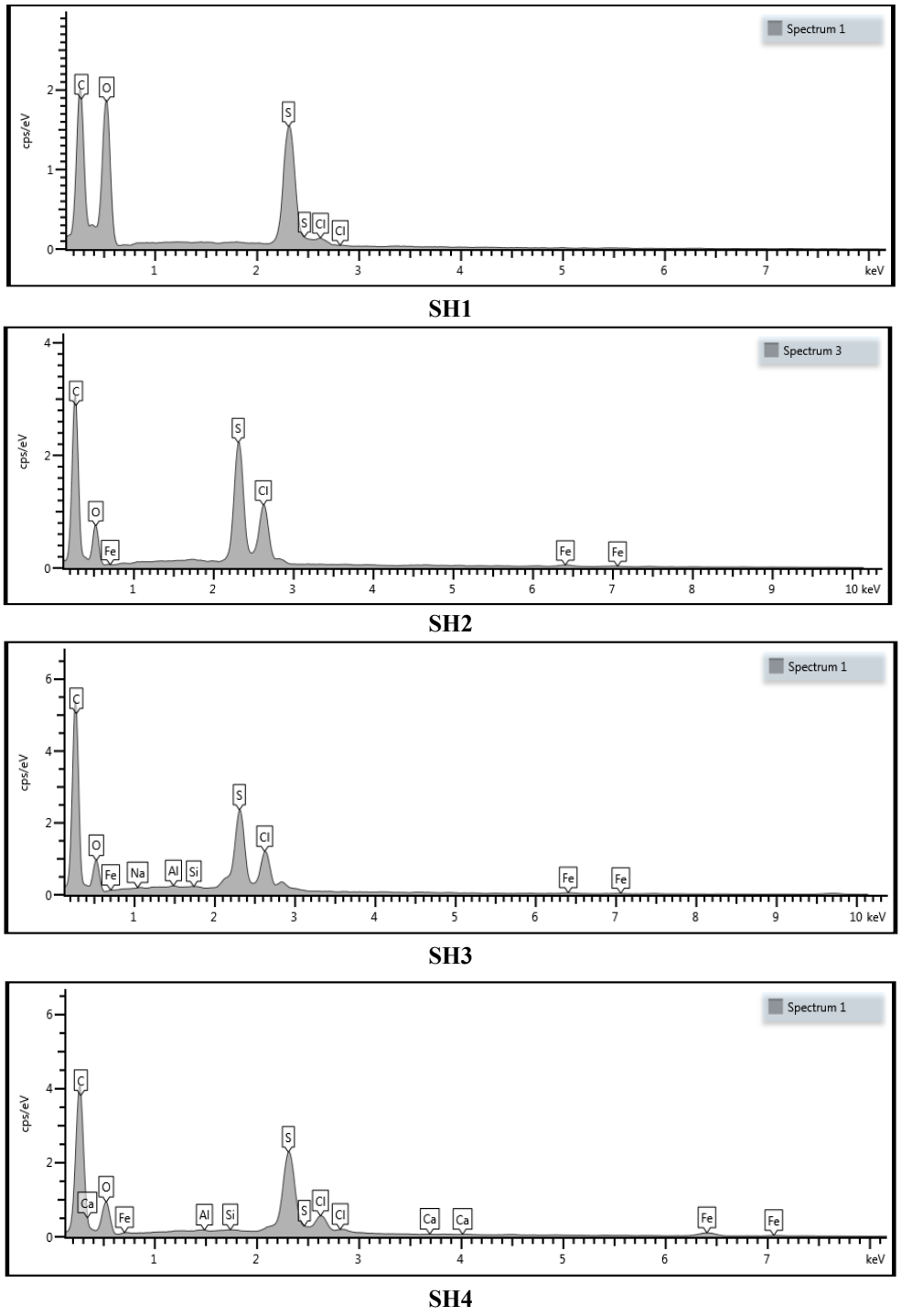

SH1

SH2

SH3

SH4

Figure 15. Energy-dispersive X-ray spectroscopy (EDS) test of PANI/iron oxide composites

Table 6. Sensing properties for NH_3 gas of thin samples

Samples	Sensitivity %	Response Time (sec)	Recovery Time (sec)
SH1	47.83	60	44
SH2	76.56	56	40
SH3	86.96	48	48
SH4	84.62	64	36

Table 6 shows the NH_3 sensing properties of α-Fe_2O_3/PANI samples. The highest sensitivity was observed for SH3, the composite (PANI + 3% α-Fe_2O_3), with a value of 86.96%, a response time of 48 s, and a recovery time of 48 s, which is attributed to the nanocrystalline phase. The chemically prepared PANI nanofiber films exhibit high surface roughness, providing a large surface area that enhances NH_3 adsorption. The high sensitivity, fast response, and short recovery times can be explained by the catalytic role of the α-A-Fe_2O_3 nanoparticles, which facilitate the decomposition of gas molecules into free radicals and enhance their interaction with oxygen and functional groups on the polymer surface. So, the behavior of 3% α-Fe_2O_3/PANI (SH3 sample) is optimal as an NH_3 gas sensor, as explained based on the following points:

A) Structurally (XRD test): The composite with a 3% nanoparticle ratio exhibits the best performance, as the well-ordered A-Fe_2O_3 provides stable conduction pathways within the amorphous PANI structure. This ratio promotes moderate crystal growth (19.99 nm), contributing to enhanced gas sensing performance. While the crystal growth was weak at 1% doping ratio (15.95 nm), the 5% nanoparticle composite shows more agglomeration and defects (19.95 nm), which likely block or cover active sites in the polymer, resulting in reduced gas sensing performance.

B) Chemically (FTIR): The results confirmed the successful synthesis of metal oxide NPs/PANI composites. The strong interfacial interaction between PANI and α-A-Fe_2O_3 is evident from the high vibrational intensity of the Fe–O bond and shifts in PANI bonds such as C=N and C–N. The optimal interaction was observed at 3%, which demonstrated a balanced structural integration, favorable for enhancing charge transfer and improving NH_3 sensing performance.

C) Morphologically (SEM test): The image of SH3 shows the most uniformity compared to other doping ratios. In addition, the images confirmed the high surface interconnected paths that enhanced the charge transfer and provided numerous active sites. Compared to other doping ratios, which either provide few active sites with disconnected paths as in low doping ratio (1%) or show the particles agglomeration leading to blocking these sites and reducing and preventing charge transfer as in high doping ratio (3%).

D) Optically (Energy gap): The main reason for the best NH_3 sensing activity is the optimal combination of film thickness (230.1 nm), dopant ratio, and the band gap value 1.96 eV). At this ratio, the p-n heterojunction depletion layer occupies most of the film, leading to the strong NH_3-induced modulation of the interfacial barrier, and this did not happen either in low or high doping ratios. The effective response of this doping ratio can mainly be attributed to the balanced film structure rather than the lowest Eg alone.

E) Electrically (Hall effect test): 3% α-A-Fe_2O_3 ratio show the highest conductivity (7.99×10^{-8} S/cm) compared to other doping ratios due to its well-dispersed nature within the PANI matrix, and strong interactions between these particles and the nitrogen atoms of PANI lead to the formation of new defect states, known as localized energy levels. These levels enhance conductivity and improve the gas sensing performance.

F) Ultimately, these combined advantages translate into the highest sensitivity, fastest response/recovery (48 s for both times response and recovery).

3.8 Discussion on the charge carrier type

The nanocomposites' electronic characterization shows the difference between surface sensing behavior and bulk transport related to sensor type, whether n-type or p-type. Whereas, the Hall effect results confirmed negative Hall coefficient values of all samples, including pure PANI ($R < 0$), indicating an n-type semiconductor. The NH_3 sensing behavior of the same samples showed a characteristic p-type response (the resistance increased with increasing exposure time of reducing gas). This phenomenon can be justified by the roles of Hematite as the core and with PANI as the shell as follows:

1. PANI as an n-type semiconductor: Although PANI is usually classified as p-type, in this work, it appeared as n-type according to Hall effect measurements. This can first be attributed to complex conduction mechanism. In a disordered polymer like PANI, the sign of the Hall coefficient does not match with the bulk charge carrier because of the hopping transport mechanism, besides the existence of bipolaronic and polaronic states. The second reason is that the Hall coefficient changes to reversed charge because of high levels of structural disorder or due to a specific arrangement of PANI chains, leading to n-type-like electronic transport characteristics in the bulk despite the p-type chemical nature of PANI in sensing performance. This behavior is matched with the results that were confirmed in Rajyalakshmi et al. [24]
2. Relating to nanocomposites, α-Fe_2O_3 acts as an n-type compound because of its oxygen vacancies. Whereas, PANI-based emeraldine salts are p-type. Upon contact, an n-p heterojunction is created at interference points. The metal oxide (α-Fe_2O_3) electrons diffuse into PANI layers, and at the same time, PANI holes diffuse into the metal oxide, forming a depletion at contact points. So, in such hybrid systems, α-Fe_2O_3 electrons move toward p-type PANI to equalize the Fermi level for the depletion region. While the bulk n-type core behaves as n-type in magnetic field measurements, the electrical percolating bath for NH_3 sensing is controlled by p-type surface and heterojunction barriers matched with the results of Bandgar et al. [25].
3. Relating to NH_3 sensing, it is noticed that samples act as p-type semiconductors with increasing resistance values, which is attributed to two mechanisms. The

first one is PANI deprotonation, in which ammonia gas acts as a strong base to react with the protonated imine in the PANI backbone and consumes the positive holes, leading to a rise in resistance. The second reason for resistance increasing is because of depletion layer expansion when NH_3 reduces the PANI positive hole concentration, leading to the depletion layer expansion at α-Fe_2O_3/PANI interference points. This expansion will narrow the conductive channels between successive chains and grains, leading to resistance increasings and this is correlated with the interpretation of Li et al. [26] in their work.

4. CONCLUSIONS

The key conclusions can be summarized as follows:

1. Polyaniline/α-A-Fe_2O_3 nanocomposite thin films were synthesized on glass substrates using oxidative polymerization and the chemical bath deposition (CBD) technique. Three doping ratios were utilized (1 wt.%, 3 wt.%, and 5 wt.%).
2. The average crystallite size of pure PANI is 15.68 nm, while that of the composites is 15.95 nm for 1% Fe_2O_3, 19.99 nm for 3% Fe_2O_3, and 19.94 nm for 5% Fe_2O_3.
3. Polyaniline thin films were characterized using UV-vis and FTIR spectroscopy. The spectra revealed both weak and strong absorption bands, indicating that the films have a high absorption coefficient in the short-wavelength range. Additionally, the absorption coefficient increased with increasing film thickness.
4. Hall measurements indicated that most of the prepared samples are n-type semiconductors.
5. The fabricated sensors exhibited good sensitivity to NH_3 gas at room temperature, with the highest sensitivity observed for sample SH3, the composite (PANI + 3% α-Fe_2O_3).

COMPETING INTERESTS AND FUNDING

The authors declare no competing financial interests. In addition, they declare that the work is self-funded work.

REFERENCES

[1] Ravi, S.S., Osipov, S., Turner, J.W. (2023). Impact of modern vehicular technologies and emission regulations on improving global air quality. Atmosphere, 14(7): 1164. https://doi.org/10.3390/atmos14071164

[2] Panda, S., Mehlawat, S., Dhariwal, N., Kumar, A., Sanger, A. (2024). Comprehensive review on gas sensors: Unveiling recent developments and addressing challenges. Materials Science and Engineering: B, 308: 117616. https://doi.org/10.1016/j.mseb.2024.117616

[3] Zhou, X., Zhou, X., Wang, C., Zhou, H. (2023). Environmental and human health impacts of volatile organic compounds: A perspective review. Chemosphere, 313: 137489. https://doi.org/10.1016/j.chemosphere.2022.137489

[4] Atafar, Z., Sarkhoshkalat, M.M., Manesh, M.B. (2025). Overview of air pollution: History, sources and effects. In Air Pollution, Air Quality, and Climate Change, pp. 1-21. https://doi.org/10.1016/B978-0-443-23816-1.00005-7

[5] Chabukswar, V.V., Bora, M.A., Adhav, P.B., Diwate, B.B., Salunke-Gawali, S. (2019). Ultra-fast, economical and room temperature operating ammonia sensor based on polyaniline/iron oxide hybrid nanocomposites. Polymer Bulletin, 76(12): 6153-6167. https://doi.org/10.1007/s00289-019-02703-4

[6] Wyer, K.E., Kelleghan, D.B., Blanes-Vidal, V., Schauberger, G., Curran, T.P. (2022). Ammonia emissions from agriculture and their contribution to fine particulate matter: A review of implications for human health. Journal of Environmental Management, 323: 116285. https://doi.org/10.1016/j.jenvman.2022.116285

[7] Walker, V. (2014). Ammonia metabolism and hyperammonemic disorders. Advances in Clinical Chemistry, 67: 73-150. https://doi.org/10.1016/bs.acc.2014.09.002

[8] Butt, M.A., Piramidowicz, R. (2024). Integrated photonic sensors for the detection of toxic gasses—A review. Chemosensors, 12(7): 143. https://doi.org/10.3390/chemosensors12070143

[9] Beygisangchin, M., Baghdadi, A.H., Kamarudin, S.K., Rashid, S.A., Jakmunee, J., Shaari, N. (2024). Recent progress in polyaniline and its composites; synthesis, properties, and applications. European Polymer Journal, 210: 112948. https://doi.org/10.1016/j.eurpolymj.2024.112948

[10] Shakeel, A., Rizwan, K., Farooq, U., Iqbal, S., Altaf, A.A. (2022). Advanced polymeric/inorganic nanohybrids: An integrated platform for gas sensing applications. Chemosphere, 294: 133772. https://doi.org/10.1016/j.chemosphere.2022.133772

[11] Kaushik, P., Bharti, R., Sharma, R., Verma, M., Olsson, R.T., Pandey, A. (2024). Progress in synthesis and applications of polyaniline-coated nanocomposites: A comprehensive review. European Polymer Journal, 221: 113574. https://doi.org/10.1016/j.eurpolymj.2024.113574

[12] Yang, J., Yu, C. (2024). Fundamentals of chemical sensors and biosensors. In Machine Learning and Artificial Intelligence in Chemical and Biological Sensing, pp. 1-21. https://doi.org/10.1016/B978-0-443-22001-2.00001-9

[13] Saruhan, B., Fomekong, R.L., Nahirniak, S. (2023). High-sensitivity and-selectivity gas sensors with nanoparticles, nanostructures, and Thin films. Chemosensors, 11(2): 81. https://doi.org/10.3390/chemosensors11020081

[14] He, L., Feng, B. (2022). Principles of sensors. In Fundamentals of Measurement and Signal Analysis, pp. 189-270. https://doi.org/10.1007/978-981-19-6549-4_7

[15] Luo, S., Xu, Z., Zhong, F., Li, H., Chen, L. (2024). Doping-induced charge transfer in conductive polymers. Chinese Chemical Letters, 35(1): 109014. https://doi.org/10.1016/j.cclet.2023.109014

[16] Gaikwad, G., Patil, P., Patil, D., Naik, J. (2017). Synthesis and evaluation of gas sensing properties of PANI based graphene oxide nanocomposites. Materials Science and Engineering: B, 218: 14-22. https://doi.org/10.1016/j.mseb.2017.01.008

[17] Khan, H.U., Tariq, M., Shah, M., Iqbal, M., Jan, M.T.

(2020). Inquest of highly sensitive, selective and stable ammonia (NH3) gas sensor: Structural, morphological and gas sensing properties of polyvinylpyrrolidone (PVP)/CuO nanocomposite. Synthetic Metals, 268: 116482. https://doi.org/10.1016/j.synthmet.2020.116482

[18] Brie, M., Turcu, R., Neamtu, C., Pruneanu, S. (1996). The effect of initial conductivity and doping anions on gas sensitivity of conducting polypyrrole films to NH3. Sensors and Actuators B: Chemical, 37(3): 119-122. https://doi.org/10.1016/S0925-4005(97)80125-6

[19] Al-Hashem, M., Akbar, S., Morris, P. (2019). Role of oxygen vacancies in nanostructured metal-oxide gas sensors: A review. Sensors and Actuators B: Chemical, 301: 126845. https://doi.org/10.1016/j.snb.2019.126845

[20] Ahmed, S., Sinha, S.K. (2023). Studies on nanomaterial-based p-type semiconductor gas sensors. Environmental Science and Pollution Research, 30(10): 24975-24986. https://doi.org/10.1007/s11356-022-21218-6

[21] Mirabella, D.A., Aldao, C.M. (2024). Dependence of n-type metal-oxide gas sensor response on the pressure of oxygen and reducing gases. ACS Sensors, 9(4): 1938-1944. https://doi.org/10.1021/acssensors.3c02674

[22] Pei, J., Guo, F., Zhang, J., Zhou, B., Bi, Y., Li, R. (2021). Review and analysis of energy harvesting technologies in roadway transportation. Journal of Cleaner Production, 288: 125338. https://doi.org/10.1016/j.jclepro.2020.125338

[23] Chen, W., Zhou, Q., Wan, F., Gao, T. (2012). Gas sensing properties and mechanism of Nano-SnO_2-based sensor for hydrogen and carbon monoxide. Journal of Nanomaterials, 2012(1): 612420. https://doi:10.1155/2012/612420

[24] Rajyalakshmi, T., Pasha, A., Khasim, S., Lakshmi, M., Imran, M. (2020). Synthesis, characterization and Hall-effect studies of highly conductive polyaniline/graphene nanocomposites. SN Applied Sciences, 2: 530. https://doi.org/10.1007/s42452-020-2349-4

[25] Bandgar, D.K., Navale, S.T., Mane, A.T., Gupta, S.K., Aswal, D.K., Patil, V.B. (2015). Ammonia sensing properties of polyaniline/a-Fe2O3 hybrid nanocomposites. Synthetic Metals, 204: 1-9. https://doi.org/10.1016/j.synthmet.2015.02.032

Li, Y., Zhao, H., Ban, H., Yang, M. (2017). Composites of Fe2O3 nanosheets with polyaniline: Preparation, gas sensing properties and sensing mechanism. Sensors and Actuators B: Chemical, 245: 34-43. http://doi.org/10.1016/j.snb.2017.01.103